


Variable offsets and processing of implicit forms toward the adaptive synthesis and analysis of heterogeneous conforming microstructure

Q. Y. Hong¹ , P. Antolin², G. Elber³, and M.-S. Kim⁴

¹Hanyang University ERICA, Department of Computer Science and Engineering, Ansan, Korea

²École Polytechnique Fédérale de Lausanne, Institute of Mathematics, Lausanne, Switzerland

³Techion - Israel Institute of Technology, Department of Computer Science, Haifa, Israel

⁴Seoul National University, Department of Computer Science and Engineering, Seoul, Korea

Abstract

The synthesis of porous, lattice, or microstructure geometries has captured the attention of many researchers in recent years. Implicit forms, such as triply periodic minimal surfaces (TPMS) has captured a significant attention, recently, as tiles in lattices, partially because implicit forms have the potential for synthesizing with ease more complex topologies of tiles, compared to parametric forms. In this work, we show how variable offsets of implicit forms could be used in lattice design as well as lattice analysis, while graded wall and edge thicknesses could be fully controlled in the lattice and even vary within a single tile. As a result, (geometrically) heterogeneous lattices could be created and adapted to follow analysis results while maintaining continuity between adjacent tiles. We demonstrate this ability on several 3D models, including TPMS.

1. Introduction

The advantages of lattice based geometries in modern design are becoming apparent in more and more applications and fields. There are applications for lattices in many areas of advanced manufacturing, from lighter materials for strong enough mechanical parts, through physical structures that mimics biological behavior in medical implants, to full control over the heat flux through porous materials [WJH⁺22,ZEE23].

Additive manufacturing (AM) or 3D printing is a powerful enabling technology for realizing lattices. Graded heterogeneity and porosity are now possible in fabrication, abilities that were unthinkable using classic subtractive manufacturing technologies, that employ CNC machining. With AM capabilities, one is able to design and fabricate porous lattices and/or microstructures of great geometric complexity and even with functional graded materials and geometries [Elb23].

There are several approaches to the creation and design of lattices, from voxel based approaches, through spline parametric forms, to implicit representations. The latter are considered more versatile in the topologies that they can represent (See Figure 1 for one example). Yet, implicits are also more difficult to manage and manipulate, in many cases, compared to parametric forms. For example the display of implicits is complex as it typically requires a marching cubes-like approximation algorithm. Similarly, the analysis of implicit form is a question that only recently picked some momentum, and is also addressed here. In Figure 1, a Marching

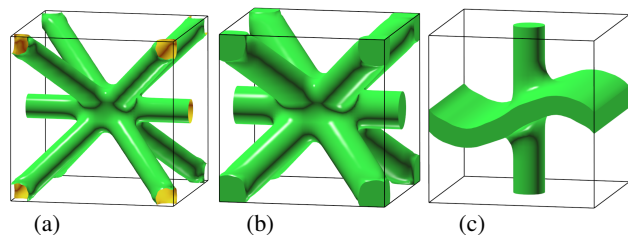


Figure 1: Variations of implicit trivariate B-spline tiles, created using a distance field from curves ((a) and (b)) and a curve and a surface (c). Considering the complexity of the central joint (with ten arms!) in (a) and (b), the recreation of a similar tile using parametric forms will be painstakingly difficult. Note the corners are forming one octant of a joint with seven other neighboring tiles. (b) and (c) shows a closed implicit tile whereas in (a) the tile is created open (so it can be connected to some neighbors).

Cubes [LC87] variant was employed to extract a displayable approximated form of this implicit B-spline trivariate tile.

The difficulties in using implicit forms compared to parametric forms are a major reason why all modern Computer Aided Geometric Design (CAD) systems are based almost solely on parametric spline forms. Yet, the topological versatility of implicits makes them a favorable solution in tiles' design, and in the exploitation of discrete topological optimization results. In addition, leveraging on novel unfitted (or immersed) finite element discretization techniques, implicits can be directly applied as geometric descriptions

for simulation purposes. However, when looking for geometric variations within created lattices or even within constructed tiles, wall thicknesses and edge diameters must be controlled as well. In this respect, one relevant fundamental difficulty in using implicit forms is the difficulty of computing offsets, not to say graded (variable) distance offsets. In order to create functionally graded geometries in implicit lattices, the wall thicknesses and edge diameters of the implicit must vary between tiles and even within a single tile. This inter-tile variable wall thickness offset as well as intra-tile variable offset is hence highly desired and is the aim of this work.

Given an implicit form $\mathcal{I}(u, v, w) = c_0$, one might argue that by adjusting the constant level c_0 , the wall thickness of the implicit form can be controlled. Unfortunately, and due to the fact that the magnitude of the gradients of implicit forms are rarely constant, not to say unit size, level set values cannot be employed to control precise offsets. In general, there is no simple global relation between the value of c_0 and an offset amount or desired wall-thickness, as the (magnitudes of the) gradients can vary arbitrarily across the domain. See Figure 2 for a counter example.

By solving the eikonal equation: $|\nabla \mathcal{I}(u, v, w)| = 1$, one may aim to approximate the offset surface in the form of $\mathcal{I}(u, v, w) = c_0 + d$, which requires a numerical integration over the region bounded by two surfaces: $\mathcal{I}(u, v, w) = c_0$ and $\mathcal{I}(u, v, w) = c_0 + d$ [Zha05]. However, the offset surface is defined more efficiently using only the given surface $\mathcal{I}(u, v, w) = c_0$ and its normal field $\nabla \mathcal{I}(u, v, w)$ of the surface. In fact, the offset surface can be approximated precisely by sampling the distances to the surface from the neighborhood of the offset surface. We employ the B-spline multivariate function which is very useful for this purpose due to the local shape control properties.

The rest of this work is organized as follows. In Section 2, we discuss relevant previous work, mostly on implicit tiles in lattice design. Section 3 portrays the different algorithms we employ in building implicit B-spline forms. In Section 3.1, we present simple ways to build implicit B-spline trivariates, for instance, using distance fields and in Section 3.2 we show how to compute constant and variable offsets of implicit forms. However, herein the implicit tiles are mapped through a trivariate form $\mathcal{T}(u, v, w)$, creating a lattice in the shape of \mathcal{T} , in Euclidean *lattice space*. As a result, constant (and variable) offsets of implicit tiles in the domain of \mathcal{T} will no longer be preserved, after the mapping through \mathcal{T} , in its *lattice space* range. In Section 3.3, we hence explore how to compute constant and variable offsets in the range of \mathcal{T} , in the Euclidean lattice space. In Section 4, we discuss (along with Appendix A) an immersive approach toward the finite element simulation on implicitly defined domains and lattices, closing the loop between design and analysis. Then, in Section 5, some results are demonstrated, including of analyses of the synthesized geometries. Finally, in Section 6, we conclude.

2. Previous Work

Additive manufacturing introduces new technologies for modeling and fabricating heterogeneous volumetric models with microstructures [YRL*19]. Triply periodic minimal surfaces (TPMS) are based on implicit representations for microstructures populated

within repetitive cuboid volume elements. The thickness of these microstructures is often controlled by the level set threshold parameters (that we just showed do not correspond to offsets) for their implicit representations [HL21, FLLF21, GCDL22, GGL24, LAR*21, MSA*18, YL23]. Hu and Lin [HL21] proposed an approach that represents the threshold as a trivariate B-spline function, called a *threshold distribution field (TDF)*. Using porous synthesis and implicit B-spline functions, Gao et al. [GCDL22, GGL24] approximated porous structures more general than those based on TPMS models. This reliance on the threshold level has little geometric meaning and it is difficult to (locally) control the thicknesses using it. As an alternative, by employing geometric operations such as minimum distance and offset computations, one can take a systematic approach that is based on the Euclidean distance field from the microstructure surfaces, which can be interpreted as variable-radius offsets from the implicit surfaces that bound the microstructures.

Implicit modeling is a method of choice for representing complex 3D shapes with non-trivial topologies and branching structures such as trees and blood vessels [Bli82, Blo95, PFV*11, WGG99, ZBQC13]. This is demonstrated, for example, in the commercial software of nTopology that provides handy and robust tools for modeling and fabricating microstructures in many industrial and biomedical applications in practice [nTo]. At the core of the new approach of implicit modeling is the power of computing Euclidean distance fields in a highly reliably way, often with the hardware support of modern GPUs. Using distance fields sampled at high resolutions, Boolean and offset operations become considerably easier and more robust to implement than other conventional methods. Nevertheless, the resolutions are yet limited and it is still quite cumbersome to support local modifications to the objects under a shape design process.

In this work, and in an effort to deal with the issue of discrete resolutions, we employ implicit B-spline functions in a more general modeling environment such as the functional mapping of implicit models [HE21, HEK23, ME16, MMAE18, MAE19]. Though yet an approximation method for the (variable-radius) offset surface construction, the problem itself poses multi-sided technical challenges due to the underlying multi-step non-linear representations as the result of composition of B-spline functions and constraints, etc.

Efficient and numerically stable computation of offsets for curves and surfaces play an important role in many geometric operations (such as rounding, filleting, and shelling) for solid modeling [BFK92, HL93, RR86]. Conventional offset algorithms mostly deal with parametric curves and surfaces that form the boundary of solid objects [CRE01, HL93]. Unfortunately, the offsets of rational curves and surfaces are algebraic, but not rational in general, except for some special cases [Far08]. This fundamental limitation has motivated the development of a large body of alternative methods that approximate offset curves and surfaces in rational forms. There have also been a few previous methods that represent the exact offsets as algebraic curves and surfaces (which are implicitly defined by polynomial equations) [Hof89]. The main computational bottleneck in this direct approach is in the algebraic degrees of the exact offsets, which are considerably higher than the given curves and surfaces. Due to the high degrees of the exact offsets, many redun-

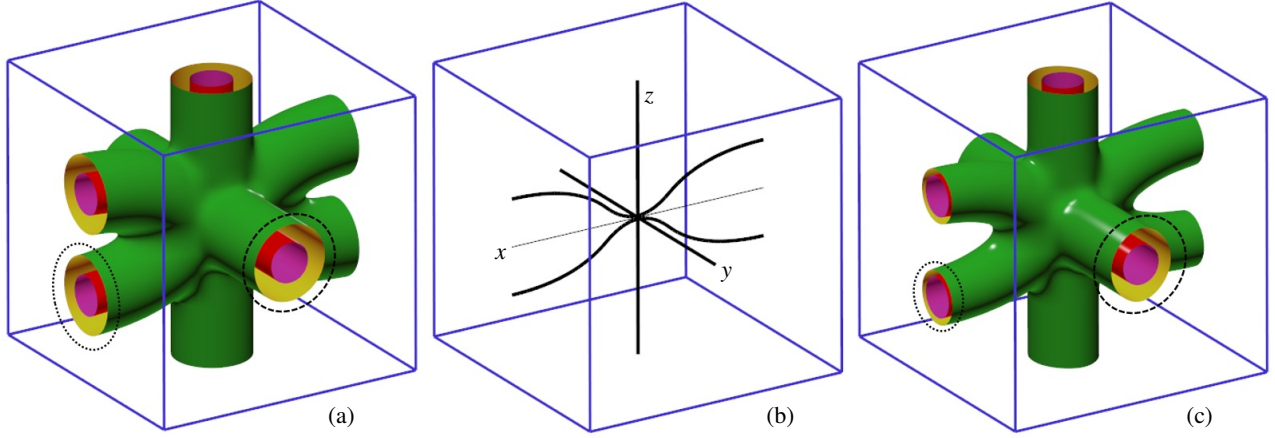


Figure 2: A counter example showing why level sets cannot be employed to compute precise offsets. The distance field to the four curves in (b) is used to derive the two different implicit trivariates in (a) and (c), that are identical at level set c_0 and shown in red as $\mathcal{I}(u, v, w) = c_0$ (interior in magenta). Adjusting the level sets, in (a) and (c), from c_0 to c_1 , yields the result in green as $\mathcal{I}(u, v, w) = c_1$ (interior in yellow). The green level set in (c) is different from (a) due to graded scaled up gradients, in (c) as we move away from the origin, along x . Note the pairs of green arms in $+x$ (in the dotted ovals) that are much closer to the original red arms in (c), compared to (a), while other arms are similar (e.g., in the dashed ovals).

dant components are often generated, which are extremely difficult to deal with, in the offset trimming procedure.

The exact offsets of implicit polynomial curves and surfaces are also high-degree algebraic curves and surfaces with many redundant components. For non-polynomial implicit surfaces such as triply periodic minimal surfaces (TPMS) defined with trigonometric functions, the exact offsets are even more difficult to compute. In the current work, we consider the problem of approximating offsets of surfaces procedurally defined with functional compositions over implicitly defined surfaces in highly general forms. A typical example of such surfaces is a trivariate volume populated with repetitive tiles defined by implicit TPMS surfaces under non-linear freeform deformation [HEK23]. To give desired uniform/non-uniform thickness, optionally with local control, to these microstructure surfaces, we develop effective offset approximation methods for both constant and variable-radius offsets.

There is a long history of developing offset approximation methods [ELK97, Mae99]. However, it is yet highly non-trivial to deal with the offset trimming of removing all redundant components from the offset curve segments and surface patches thus approximated [HPKE19]. Though with somewhat limited precision of approximation, a highly effective approach for robust implementation of offset computation can be based on the computation of distance fields, such as the methods proposed by Kobbelt [PK08], Wang and Manocha [WM13], and Li and McMains [LM14]. We take a similar approach but represent the approximated distance field in a B-spline form, where the constant and variable-radius offset surfaces can be extracted by marching over the B-spline distance function defined on a trivariate volume in the Euclidean space. The representation in B-spline forms makes it easy to overcome the limited resolution of the voxelized space for sampling the distances. More importantly, the basic framework is not only limited to the Euclidean distance, and it is applicable to diverse application environments for the synthesis and analysis of heterogeneous microstructures.

Regarding simulation of lattice geometries defined through implicits, the current main limitation is the high computational cost of classical finite element discretization techniques, that are greedy in terms of computational resources. Thus, most of the available results, including some commercial solutions, are limited to either shell (2D) models [WRC*20] or a small number of tiles [AES*19]; or they apply model reduction techniques such as multiscale or numerical homogenization [KHL19], both relying on the separation of scales, what it is usually not true for most of the applications due to the achievable length-scale of current 3D printers. Worth mentioning exceptions are the works [KAH*21b, KAH*21a] in which the authors leveraged on immersed finite element techniques, similar to the ones applied in this work, for studying the behavior of printed lattice designs using images, or the Immersed Method of Moments developed by Intact Solutions and applied to the simulation of implicitly defined lattices [Sol].

3. Algorithms

Consider a parametric trivariate $\mathcal{T}(t_x, t_y, t_z) : D \rightarrow \mathbb{R}^l$, $l \geq 3$ where the 3D geometry of \mathcal{T} is defined for $1 \leq l \leq 3$ and an arbitrary set of material properties are optionally prescribed for $l \geq 4$. \mathcal{T} will be denoted the *macro-shape* hence after. One can arrange a 3D grid of implicit tiles, $\mathbf{I}_{ijk}(u, v, w)$, $u, v, w \in [0, 1]$ in domain D , so (u, v, w) of each tile affinely (up to translation and scale) equates with (t_x, t_y, t_z) , for some box sub-domain of D , (See Figure 3), only to evaluate them through \mathcal{T} , yielding a lattice in the shape of \mathcal{T} . One should note that while the direct composition of \mathbf{I}_{ijk} and \mathcal{T} is difficult, point evaluation is simple and will be denoted as $\mathcal{T}(\mathbf{I}_{ijk})$.

Now, consider one such implicit tile $\mathbf{I} \subset D$. $\mathcal{T}(\mathbf{I})$ can inherit from \mathcal{T} certain properties, such as RGB colors, and can also inherit physical properties such as local wall thicknesses and/or local diameters of arms (recall Figure 1) or even local stiffnesses. Further, local properties can also be prescribed at the tile level as

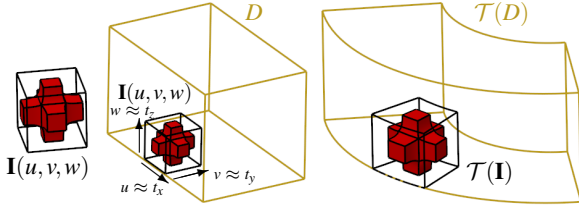


Figure 3: The relationship between an implicit trivariate tile $\mathbf{I}(u, v, w)$ and the parametric trivariate macro-shape $\mathcal{T}(t_x, t_y, t_z)$. Note that, for every tile \mathbf{I} in \mathcal{T} , the tiles' (u, v, w) parametric values affinely equates (denoted by \approx) with the parameters of a box sub-domain of the domain D of \mathcal{T} , or $(u, v, w) \approx (t_x, t_y, t_z)$, for every tile in D .

$\mathbf{I}(u, v, w) : [0, 1]^3 \rightarrow \mathbb{R}^m$, where \mathbf{I}^1 defines the implicit geometry, with $\mathbf{I}^1(u, v, w) > 0$ being the interior, and $\mathbf{I}^r(u, v, w)$, for coordinate $1 < r \leq m$, optionally prescribing a variety of local tile properties.

Properties that are described at the tile level are going to be repeated throughout the lattice for all tiles. If a tile's property is periodic at the tile level[†], the property will be periodic throughout the lattice. In contrast, properties that are prescribed by \mathcal{T} will preserve the continuity of the entire shape (following the continuity of \mathcal{T}) while being of possibly completely different values for different tiles (locations). See [HEK23] for more on implicit tiles in trivariate based lattices.

The design of lattices using implicit tiles entails several steps, starting from the creation of implicit B-spline trivariate tiles, that is discussed in Section 3.1. Then, the synthesis of constant- and variably-controlled distance offsets of implicits, in individual tile, is discussed in Section 3.2. Mapping the tiles through the macro-shape \mathcal{T} , a constant offset will no longer be preserved and in Section 3.3, we also consider constant- and variably-controlled offsets in Euclidean lattice space, after the mapping through macro-shape \mathcal{T} .

3.1. Creating implicit tiles

We focus here on implicit trivariate B-spline tiles that are created in one of the following possible ways:

- **Distance fields.** Consider a set of space curve and surface entities E_q as $C_q(t_q)$ and $S_q(t_q, r_q)$, in $[0, 1]^3$. Let $d_q^{\min}(p) = \min_{t_q} \|p - E_q\|$ be the minimum distance between space point p and entity E_q . Then, let $D_q^{\min}(p) = \min_q d_q^{\min}(p)$, or the minimum distance between p and all entities $C_q(t_q)$ and $S_q(t_q, r_q)$. Now consider a scalar B-spline trivariate of general degrees (d_u, d_v, d_w) :

$$\mathbf{I}(u, v, w) = \sum_{i=0}^{n_u-1} \sum_{j=0}^{n_v-1} \sum_{k=0}^{n_w-1} p_{ijk} B_i^{d_u}(u) B_j^{d_v}(v) B_k^{d_w}(w) \quad (1)$$

with $(n_u \times n_v \times n_w)$ coefficients and $u, v, w \in [0, 1]$. Assuming a

[†] A property is considered *periodic at the tile level* if it is identical for opposite tile boundaries; for example of same values for $u = 0$ and $u = 1$

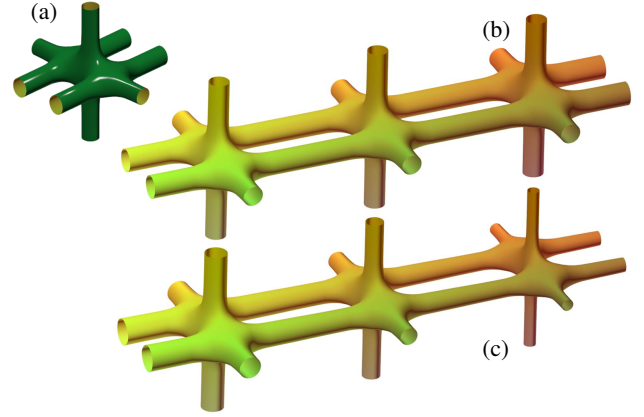


Figure 4: Two examples of three implicit tiles in a row. The basic tile is shown in (a) built using the distance field implicit tile creation approach, and empty four orthogonal lines (two of which are, in fact, parallel). The tiles are created uniform geometrically in (b) and graded geometrically in (c). Both are created heterogeneous with respect to material (color). Each tile is a tri-quadratic B-spline with 10 control points in each direction.

uniform spacing of coefficients in a 3D grid in $[0, 1]^3$, coefficient p_{ijk} is located at $\left(\frac{i}{n_u-1}, \frac{j}{n_v-1}, \frac{k}{n_w-1}\right)$.

Set p_{ijk} to be $p_{ijk} = D_q^{\min}\left(\frac{i}{n_u-1}, \frac{j}{n_v-1}, \frac{k}{n_w-1}\right)$. By spline approximation properties, $\mathbf{I}(u, v, w) = d_0$ is now an implicit B-spline trivariate that approximates the iso-distance d_0 from $C_q(t_q)$ and $S_q(t_q, r_q)$.

Finally, $d_q^{\min}(p) = \min_{t_q} \|p - C_q(t_q)\|$ can be computed by seeking the minimum of its square, or its vanishing derivative parametric locations:

$$0 = \frac{d(p - C_q(t_q))^2}{dt_q} = (p - C_q(t_q)) \cdot C_q'(t_q),$$

solving a non-linear equation. C_q^1 discontinuities in $C_q(t_q)$ must also be examined for the minimum, as well as the two end points of C_q . The minimum point distance to surface $S_q(t_q, r_q)$ can be similarly derived.

The tiles shown in Figure 1 were created using this approach and are approximated and displayed using marching cubes, as an open tile (in Figure 1 (a)) and as closed tiles with boundary (Figure 1 (b) and (c)). Then, Figure 4 shows two additional examples that are also graded geometrically and material-wise (color).

- **Implicit Evaluation.** Let $\mathcal{I}(u, v, w) = 0$ be an implicit function, for $u, v, w \in [0, 1]$. Reconsider $\mathbf{I}(u, v, w)$ from Equation (1), and set p_{ijk} to equal $p_{ijk} = \mathcal{I}\left(\frac{i}{n_u-1}, \frac{j}{n_v-1}, \frac{k}{n_w-1}\right)$. By the properties of Bernstein/B-spline basic functions, $\mathbf{I}(u, v, w)$ approximates \mathcal{I} (uniformly, as (n_u, n_v, n_w) converge to infinity). In other words, given any implicit function $\mathcal{I}(u, v, w) = 0$, by simply sampling \mathcal{I} , one can approximate \mathcal{I} as closely as desired, via an increase in the mesh size, as $\mathbf{I}(u, v, w) = 0$. Figure 5 shows an example of sampling a TPMS Gyroid function into an implicit tri-quadratic B-spline function of size $10 \times 10 \times 10$.
- **Implicit least squares.** As an alternative to Implicit Evaluation,

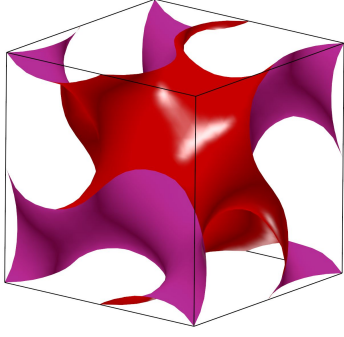


Figure 5: An implicit tri-quadratic B-spline function of size $10 \times 10 \times 10$ approximating a Gyroid function tile by sampling.

one can aim to best fit the B-spline trivariate to a given implicit function $\mathcal{I}(u, v, w) = 0$.

In this method, the coefficients p_{ijk} 's in $\mathbf{I}(u, v, w)$ from Equation (1) are determined by minimizing E , the sum of squared distances between $\mathbf{I}(u, v, w)$ and $\mathcal{I}(u, v, w)$, formulated as follows.

$$E = \sum_{m=1}^M (\mathbf{I}(u_m, v_m, w_m) - \mathcal{I}(u_m, v_m, w_m))^2$$

where M , being larger than the number of coefficients, is the number of point samples for fitting, and u_m, v_m, w_m are in $[0, 1]$. The least square problem is formulated by finding p_{ijk} 's that satisfy $\frac{\partial E}{\partial p_{ijk}} = 0$ for all i, j , and k , or

$$\sum_{m=1}^M (\mathbf{I}(u_m, v_m, w_m) - \mathcal{I}(u_m, v_m, w_m)) \cdot \frac{\partial \mathbf{I}(u_m, v_m, w_m)}{\partial p_{ijk}} = 0,$$

and can be solved via direct methods.

Hu and Lin [HL21] proposed the Least Square Progressive and Iterative Approximation (LSPIA) method to fit a scalar B-spline trivariate to the implicit function in an iterative manner. This method initializes p_{ijk} 's to zero and updates the values of p_{ijk} 's iteratively until they converge, by distributing the error of the m -th sample to the coefficients in $\mathbf{I}(u, v, w)$ that contribute to evaluation of the sample, with a weight of $B_i^{d_u}(u_m)B_j^{d_v}(v_m)B_k^{d_w}(w_m)$.

In all these tiles' construction schemes, continuity must be preserved between adjacent trivariate tiles. Hence, typically, for C^0 continuity, open-end conditions can be employed and the coefficients of adjacent trivariates are made identical on the shared boundary faces. Further, if the offset is constant, a simple alternative is to impose periodic boundary conditions on the fitted spline.

3.2. The Creation of variable distance offsets of Implicit

Consider the implicit tile $\mathbf{I}(u, v, w)$ and let the steepest ascent/descent direction of \mathbf{I} , be $(V_u, V_v, V_w) = \frac{\nabla \mathbf{I}}{|\nabla \mathbf{I}|}$, where $\nabla \mathbf{I}$ is the gradient of \mathbf{I} . Then, using a first order Taylor series expansion,

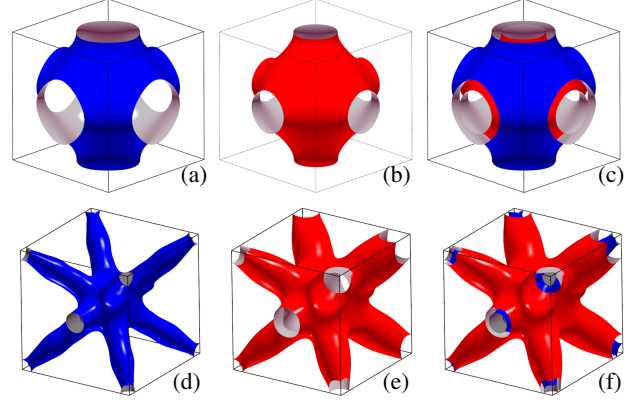


Figure 6: An implicit trivariate TPMS (Schwarz-P) approximation tile (created using an interpolatory fitting scheme similar to [HL21]) in (a) and an implicit trivariate 3D cross tile (created using a distance field to curves) in (d) are employed to demonstrate (the zero sets of the) variable distance offset computations, as are shown in (b) and (e). (c) and (f) show (the zero sets of the) implicit of the base as well as the variable distance offset implicit, in the same images.

$$\begin{aligned} & \mathbf{I}(u + dV_u, v + dV_v, w + dV_w) \\ &= \mathbf{I}(u, v, w) + \frac{\partial \mathbf{I}}{\partial u} dV_u + \frac{\partial \mathbf{I}}{\partial v} dV_v + \frac{\partial \mathbf{I}}{\partial w} dV_w + O(d^2) \\ &\simeq \mathbf{I}(u, v, w) + d \left(\frac{\partial \mathbf{I}}{\partial u}, \frac{\partial \mathbf{I}}{\partial v}, \frac{\partial \mathbf{I}}{\partial w} \right) \cdot (V_u, V_v, V_w) \\ &= \mathbf{I}(u, v, w) + d \nabla \mathbf{I} \cdot \frac{\nabla \mathbf{I}}{|\nabla \mathbf{I}|}. \end{aligned} \quad (2)$$

Now d can prescribe (a first order approximation of) the offset distance. Further, d can be a function of u, v, w as $d(u, v, w)$ and hence Equation (2) can also represent variable distance inter-tiles offset but also intra-tile offset! Then, \mathbf{I}_d , a first order approximation of the variable distance offset of \mathbf{I} by $d(u, v, w)$ can now be represented as the new implicit

$$\mathbf{I}_d(u, v, w) = \mathbf{I}(u, v, w) + d(u, v, w) \frac{\nabla \mathbf{I} \cdot \nabla \mathbf{I}}{|\nabla \mathbf{I}|}. \quad (3)$$

Now $\mathbf{I}(u, v, w)$ and $\mathbf{I}_d(u, v, w)$ form together a new tile of a certain, possibly variable, thickness. Considering the material between $\mathbf{I}(u, v, w)$ and $\mathbf{I}_d(u, v, w)$ and we have formed a tile of (variable) controlled wall thickness. Further and alternatively, one can employ $\mathbf{I}_{-d}(u, v, w)$ and $\mathbf{I}_{+d}(u, v, w)$ to achieve a symmetric tile around $\mathbf{I}(u, v, w)$.

Figure 6 shows two examples, of an implicit TPMS (Schwarz-P) tile in Figure 6 (a) and of an implicit B-spline trivariate in (d). (b) and (e) show the results of (the zero sets of the) variable distance offsets computed using Equation (3), whereas (c) and (f) show together (the zero sets of) the base implicit tiles and their respective variable distance offset implicit, in the same images.

3.3. Constant-/variably-controlled offsets in lattice space

While in the previous section, we presented an approach to compute constant- and variably-controlled offsets of implicit, by mapping the offset implicit through the *macro-shape* \mathcal{T} , the offset distances are not likely to be preserved. Further, by computing offsets of individual tiles that are C^0 continuous, offsets of those tiles will no longer be continuous. Herein, we aim to alleviate these difficulties by:

- Estimations of offset distances in Euclidean space and after the mapping through \mathcal{T} took place.
- Fitting a single implicit spline for the entire lattice, ensuring any desired continuity throughout.
- Topological changes in the tiles and throughout the lattice could be accommodated in a simple way, including due to infinitesimal offset changes.

For some specific tile $\mathcal{I}(u, v, w)$ in \mathcal{T} , $\mathcal{T}(t_x, t_y, t_z)$ is $\mathcal{T}(u, v, w)$ as (u, v, w) and (t_x, t_y, t_z) equate. Thus, given a generic point $\mathbf{x} = \mathcal{T}(t_x, t_y, t_z) = \mathcal{T}(u, v, w)$, we denote as $\bar{\mathbf{x}}$ its closest point such that its pre-image lays on the surface $\mathcal{I}(u, v, w) = 0$, i.e., $\mathcal{I}(\mathcal{T}^{-1}(\bar{\mathbf{x}})) = 0$ (see Figures 7 (a)-(b)). The computation of $\bar{\mathbf{x}}$ will be addressed below. In this way, the new geometry is defined as region between the implicit functions \mathbf{I}_{+e} and \mathbf{I}_{-e} , defined as:

$$\mathbf{I}_{+e}(u, v, w) = \text{dist}_{\pm}(u, v, w) + d, \quad (4a)$$

$$\mathbf{I}_{-e}(u, v, w) = \text{dist}_{\pm}(u, v, w) - d, \quad (4b)$$

where $\text{dist}_{\pm}(u, v, w)$ is the signed distance between the points \mathbf{x} and $\bar{\mathbf{x}}$, and it is defined as

$$\text{dist}_{\pm}(u, v, w) = \text{sign}(\mathcal{I}(u, v, w)) \|\mathcal{T}(u, v, w) - \bar{\mathbf{x}}(u, v, w)\|. \quad (5)$$

The resulting functions \mathbf{I}_{+e} and \mathbf{I}_{-e} for a Schwarz-P tile example is shown are Figure 7 (d), and after composition with a trivariate function \mathcal{T} in Figure 7 (e). As before, the offset distance d with respect to the mid-surface $\mathcal{I}(u, v, w) = 0$ can be a function of u, v, w and can be chosen separately for \mathbf{I}_{+e} and \mathbf{I}_{-e} . Actually, it can be appreciated that to achieve a constant offset in Figure 7 (e), the offsets in the domain D (Figure 7 (d)) are non constant. The functions \mathbf{I}_{+e} and \mathbf{I}_{-e} can be further approximated as B-spline trivariates by using any of the methods proposed in Section 3.1.

The question of finding the closest point $\bar{\mathbf{x}}$ remains open. For a given point $\mathbf{x}(u, v, w)$, this can be formulated as a constrained minimization problem:

$$\begin{aligned} (\bar{u}, \bar{v}, \bar{w}) &= \arg \min_{t_x, t_y, t_z} \|\mathcal{T}(t_x, t_y, t_z) - \mathbf{x}\| \\ \text{s.t. } \mathcal{I}(\bar{u}, \bar{v}, \bar{w}) &= 0 \text{ and } \bar{\mathbf{x}} = \mathcal{T}(\bar{u}, \bar{v}, \bar{w}). \end{aligned} \quad (6)$$

For solving such constrained optimization problem, similarly to [Say14], we recast it as: Find $(\bar{u}, \bar{v}, \bar{w}, \bar{\mu})$ such that

$$(\bar{u}, \bar{v}, \bar{w}, \bar{\mu}) = \arg \min_{t_x, t_y, t_z, \lambda} f(t_x, t_y, t_z, \lambda), \quad (7)$$

where $f: \mathbb{R}^3 \times \mathbb{R} \rightarrow \mathbb{R}$ is the functional given by[†]:

$$f(t_x, t_y, t_z, \lambda) = \frac{1}{2} \|\mathcal{T}(t_x, t_y, t_z) - \mathbf{x}\|^2 + \lambda \mathcal{I}(t_x, t_y, t_z), \quad (8)$$

[†] The method originally proposed in [Say14] can be seen as a particularization for the case in which the macro-shape \mathcal{T} is the identity.

and λ is a Lagrange multiplier that constrains the closest point to be in the zero level set of $\mathcal{I}(t_x, t_y, t_z)$. The saddle-point of this functional is sought by means of an iterative Newton-Raphson algorithm starting from an initial guess $\mathbf{w}_0 = (\bar{u}_0, \bar{v}_0, \bar{w}_0, \bar{\mu}_0)$, where successive approximations are computed as:

$$\mathbf{w}_{i+1} = \mathbf{w}_i - \left(\nabla^2 f(\mathbf{w}_i) \right)^{-1} \nabla f(\mathbf{w}_i). \quad (9)$$

The functional's gradient is:

$$\nabla f = \left((\mathcal{T}(t_x, t_y, t_z) - \mathbf{x}) \frac{\nabla \mathcal{T}(t_x, t_y, t_z)}{\mathcal{I}(t_x, t_y, t_z)} + \lambda \nabla \mathcal{I}(t_x, t_y, t_z) \right) \quad (10)$$

and its Hessian:

$$\nabla^2 f = \begin{pmatrix} \nabla^2 f_{x,y,z} & \nabla \mathcal{I}(t_x, t_y, t_z) \\ \nabla \mathcal{I}(t_x, t_y, t_z) & 0 \end{pmatrix}, \quad (11)$$

where

$$\nabla^2 f_{x,y,z} = \nabla^\top \mathcal{T}(t_x, t_y, t_z) \nabla \mathcal{T}(t_x, t_y, t_z) - \mathbf{x} \nabla^2 \mathcal{T}(t_x, t_y, t_z). \quad (12)$$

The choice of the initial guess \mathbf{w}_0 is critical for the success and performance of the iterative process. For that purpose, we compute $(\bar{u}_0, \bar{v}_0, \bar{w}_0)$ by finding the closest point to \mathbf{x} in a cloud of N precomputed points $\mathbf{Y} = \left\{ \mathbf{y}_q \in \mathbb{R}^3 \mid \mathcal{I}(\mathcal{T}^{-1}(\mathbf{y}_q)) = 0 \right\}_{q=1}^N$ (see Figure 7 (c)). The points \mathbf{y}_q are created by sampling the zero level-set of \mathcal{I} in the domain D and then mapping them through \mathcal{T} . The search of the closest point in the cloud \mathbf{Y} is performed by means of the k-d tree algorithm proposed in [Say14]. The sampling of the zero level-set of \mathcal{I} in D is performed by means of the algorithms proposed in [Say22, Say15] for the generation of quadrature rules for implicit domains defined through polynomials and general C^1 analytic functions, respectively. Both algorithms, as well as the k-d tree mentioned above, are implemented in the open source project algoim [Say].

It is worth mentioning that, when placing several implicit tiles together in the domain D (recall Figure 4), for a given point \mathbf{x} belonging to the subdomain of one of the tiles, the closest point $\bar{\mathbf{x}}$ may not belong to the same subdomain, but to the one of a neighboring tile. For this reason, in the procedure detailed above, the implicit function $\mathcal{I}(x, y, z)$ must be understood as the union of the functions of all the tiles considered, that are assumed to be smooth enough at their interfaces. In addition, when approximating the resulting functions \mathbf{I}_{+e} or \mathbf{I}_{-e} as B-spline trivariates, the whole set of tiles is considered together, fitting one single B-spline for the whole domain. The order, knot sequences, and number of control points of such spline approximations can be chosen to guarantee the required continuity at the tiles' interfaces.

4. Direct Simulation of Implicit lattices

While the geometries presented above are analysis suitable, the application of traditional boundary fitted finite element methods [Hug00] for solving Partial Differential Equations (PDEs) may be cumbersome as it requires the creation of high-quality boundary-fitted parametric meshes that may be a non-trivial task. In order to overcome this difficulty, in this work we leverage on unfitted discretization techniques [BCH*15, DPYR08, MS18, BVM18].

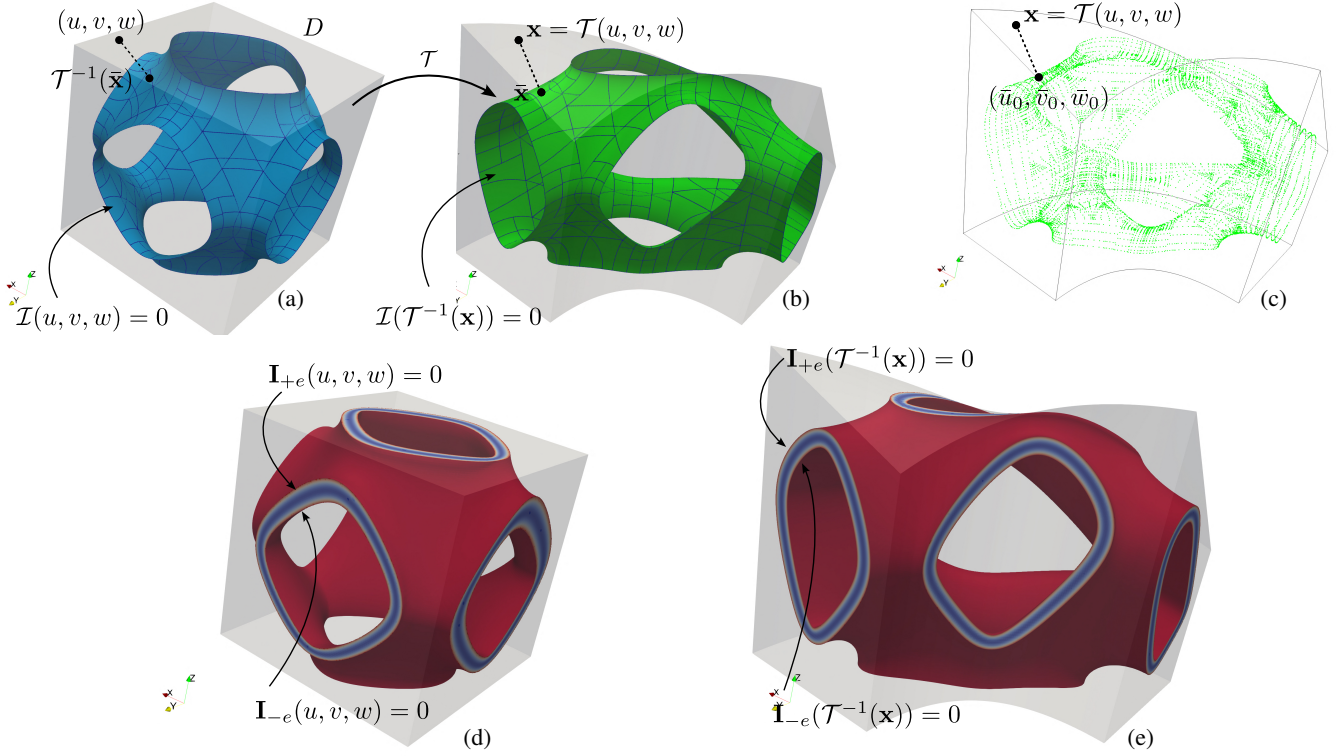


Figure 7: Creation of controlled offsets for a Schwarz-P tile in lattice space. In (a), the tile $\mathcal{I}(u, v, w) = 0$ in D is represented (through a non-conforming high-order reparametrization). In (b), the tile is mapped by a trivariate \mathcal{T} . A cloud of points lying on the mapped tile is represented in (c): these points are used for accelerating the search of the closest point $\bar{\mathbf{x}}$ to a given point \mathbf{x} . Finally, the material between \mathbf{I}_{-e} and \mathbf{I}_{+e} is represented in the domain D (in (d)) and in the lattice space in (in (e)).

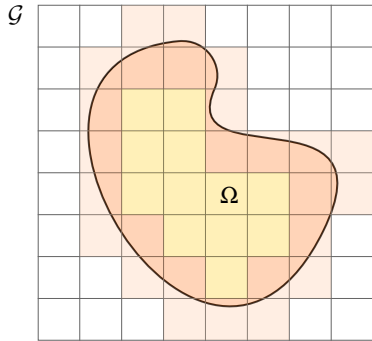


Figure 8: In unfitted finite elements methods, the computational domain to analyze Ω is immersed in a background grid \mathcal{G} , independent from the geometry, that is used to discretize the PDE solution. The elements of the grid can be classified as internal (yellow), cut (orange), or external (white).

The main idea of such family of methods is to immerse the domain Ω in a background mesh \mathcal{G} (see Figure 8) that serves as base for discretizing the PDE at hand, instead of creating a boundary-fitted discretization. Thus, following a Galerkin setting, the degrees-of-freedom and basis functions of the PDE discretized

solution and test functions are built upon the background mesh \mathcal{G} . In our case, \mathcal{G} is chosen as (a refinement of) the parametric domain partition of the implicit B-spline trivariates. Thus, \mathcal{G} is naturally split into three disjoint sets of elements, namely:

$$\mathcal{G}_{\text{in}} = \{Q \mid Q \in \mathcal{G} : Q \cap \Omega = Q\}, \quad (13a)$$

$$\mathcal{G}_{\text{out}} = \{Q \mid Q \in \mathcal{G} : Q \cap \Omega = \emptyset\}, \quad (13b)$$

$$\mathcal{G}_{\text{cut}} = \{Q \mid Q \in \mathcal{G} : Q \not\subset \mathcal{G}_{\text{in}} \cup \mathcal{G}_{\text{out}}\}. \quad (13c)$$

These three families correspond to the internal, external, and cut elements, respectively (recall Figure 8), being the PDE at hand discretized by means of finite-element techniques solely in the active part of the grid, i.e, in the internal and cut elements. Further details about the formulation of the method and the problems associated with unfitted techniques, including the treatment of cut elements, are deferred to Appendix A.

5. Experimental Results

We now present some examples of creating lattices of implicit tiles with constant and graded wall thickness as well as analyzing them.

5.1. Prescribed offsets in the domain of the macro-shape

This sub-section portrays results that employ the offset computation scheme presented in Section 3.2. Figure 9 presents a constant as well as variable size offsets of a cross tile in a torus macro-shape with a square cross section. In (a) and (b) constant offset tiles are shown, that after mapping through the macro-shape \mathcal{T} the tiles are made thicker toward the outside. (c) and (d) present a case where the thickness of the cross tiles are further varying around the torus. Note (c) and (d) also present graded material content (colors) around the torus. The cross tile was an implicit trivariate of orders $(3 \times 3 \times 3)$ and $(10 \times 10 \times 10)$ control points, and the macro shape is of orders $(4 \times 2 \times 2)$ and $(13 \times 2 \times 2)$ control points in \mathbb{R}^7 where the first three dimensions prescribes the geometry, three for the RGB color properties of the macro shape \mathcal{T} , and the last dimension prescribes the offset distance d from Equation (2). The computation times of the marching cube procedure took little over 10 seconds and little over 20 seconds for constant and variable distance offset tiles, respectively, on an Intel Core i7-12700 2.10GHz PC with 12 threads. It took longer to compute variable distance offsets than constant offsets because the marching cubes are executed as many times as the number of tiles in variable distance offsets, whereas the marching cubes' result can be shared between the tiles, for constant offset tiles.

Figures 10 to 12 show both the original lattice geometry as well as its variable distance offset of a graded material (color) duck model (Figures 10 and 11) and graded material wing model (Figure 12), with implicit cross tiles in Figures 10 and 12, and the tile from Figure 1 in Figure 11. These macro-shape geometries are trivariates of orders $(3 \times 3 \times 3)$ and $(6 \times 4 \times 10)$ control points for the duck shape, and of orders $(4 \times 2 \times 3)$ and $(4 \times 2 \times 10)$ control points for the wing shape, both defined again in \mathbb{R}^7 as in Figure 9. The computation times of the marching cube procedure for the offset tiles in the duck shape took around 25 seconds for constant offsets and close to 40 seconds for variable distance offsets. For the wing example, it took 13 seconds to compute constant offset tiles, and almost 30 seconds for variable distance offset tiles, on the same i7-12700 machine.

5.2. Prescribed offsets in Euclidean Lattice space

In this subsection, we gathered a few examples of generated lattices that present a prescribed offset in Euclidean lattice space (following the algorithm introduced in Section 3.3). A first simple example, shown in Figure 13, is designed to highlight the differences from the approach in Section 3.2. In this case, we consider an implicit tile defined by a linear function $\mathcal{I}(x, y, z) = z - 1/2$, mapped through a tapered trivariate geometry, and with a constant offset distance $d = 0.15$ in Euclidean lattice space. As can be observed, the lattice presents constant thickness on both sides of the mid-surface $z = 1/2$ and gets skewly trimmed by the tapered faces of the trivariate. In Figure 13, as well as in all the other results in the subsection, the distance to the offset surfaces in Euclidean space is visualized as a color field on top of the geometry: The distance is zero (white) on the offset surfaces and maximum (brown) on the mid-surface.

In Figure 14, we present several examples in which the Schoen's gyroid and Scharwz's diamond implicit tiles are mapped through a

torus with square cross section that has orders $(4, 2, 2)$ and $(13, 2, 2)$ control points. In the left part of the figure (i.e., Figures 14 (a) and 14 (c)) the tiles are generated with a constant offset distance $d = 0.1$ symmetrically on both sides of the mid-surface, prescribed in Euclidean lattice space; while in the right part (Figures 14 (b) and 14 (d)) the offset varies linearly and periodically along the circumferential parametric direction, from $d_{\min} = 0.1$ up to $d_{\max} = 0.28$, on both sides of the mid-surface. In Figures 14 (b) and (d), the topological changes are smoothly acomodated for the different offset amounts. No self-intersection processing is needed - examine the two marked rectangles in (b) and in (d), having different topologies in the small and the large offsets.

In all cases, the implicit offsets \mathbf{I}_{+e} and \mathbf{I}_{-e} were approximated as one single B-spline trivariate each containing all the tiles in the macro-shape. These B-spline approximations have orders $(3, 3, 3)$ and $(259, 35, 35)$ control points in \mathbb{R}^1 , with C^1 continuity at the tiles' interfaces.

In a similar way, in Figure 15, $(18, 5, 4)$ implicit tiles, with the same analytic implicit definitions as before, were mapped through a duck geometry that has orders $(3, 3, 3)$ and $(6, 4, 10)$ control points. A constant offset distance $d = 0.01$ on both sides of the mid-surface was considered in all the cases and the offsets \mathbf{I}_{+e} and \mathbf{I}_{-e} were approximated as one single B-spline trivariate each with orders $(3, 3, 3)$ and $(259, 35, 35)$ control points in \mathbb{R}^1 , with C^1 continuity at the tiles' interfaces. As it can be observed in the figures, the different size of the duck's Bézier elements, combined with the constant distance offset of the tiles, induces severe variations in the tiles' topology, with some of them (as the ones near the tail and head) almost solid.

All the examples in this subsection were computed using a single processor in an Apple M2 Max chip with 64 GB of DRAM memory. The generation of the implicit offsets \mathbf{I}_{+e} and \mathbf{I}_{-e} and their approximation with B-spline trivariates took between 0.41 and 1.24 seconds for the cases in Figure 14, and between 3.05 and 8.73 seconds for the ones in Figure 15.

5.3. Simulation

To illustrate the possibility of running finite element simulations directly using the constructed geometries, we present two examples (Figures 16 and 17) following the methodology proposed in Section 4. In both cases, we solve a linear elasticity problem (see Appendix A), setting the material mechanical properties as: Young's modulus $E = 1$ and Poisson's ratio $\nu = 0.3$. In all cases, just part of the boundary is constrained[§], the rest is traction free (homogeneous Neumann condition), and a distributed load is applied everywhere in the model.

The first test case corresponds to TPMS cross tiles as implicit trivariates that are mapped through a torus with square cross section. $(16, 2, 2)$ tiles were placed in the parametric domain of the torus, where every cross tile trivariate has orders $(3, 3, 3)$ and

[§] As detailed in A, and for the sake of simplicity, Dirichlet boundary conditions are only applied on a subset Γ_D of the boundary that is also part of the boundary of the grid \mathcal{G} , i.e., $\Gamma_D \subset \partial\Omega \cap \partial\mathcal{G}$.

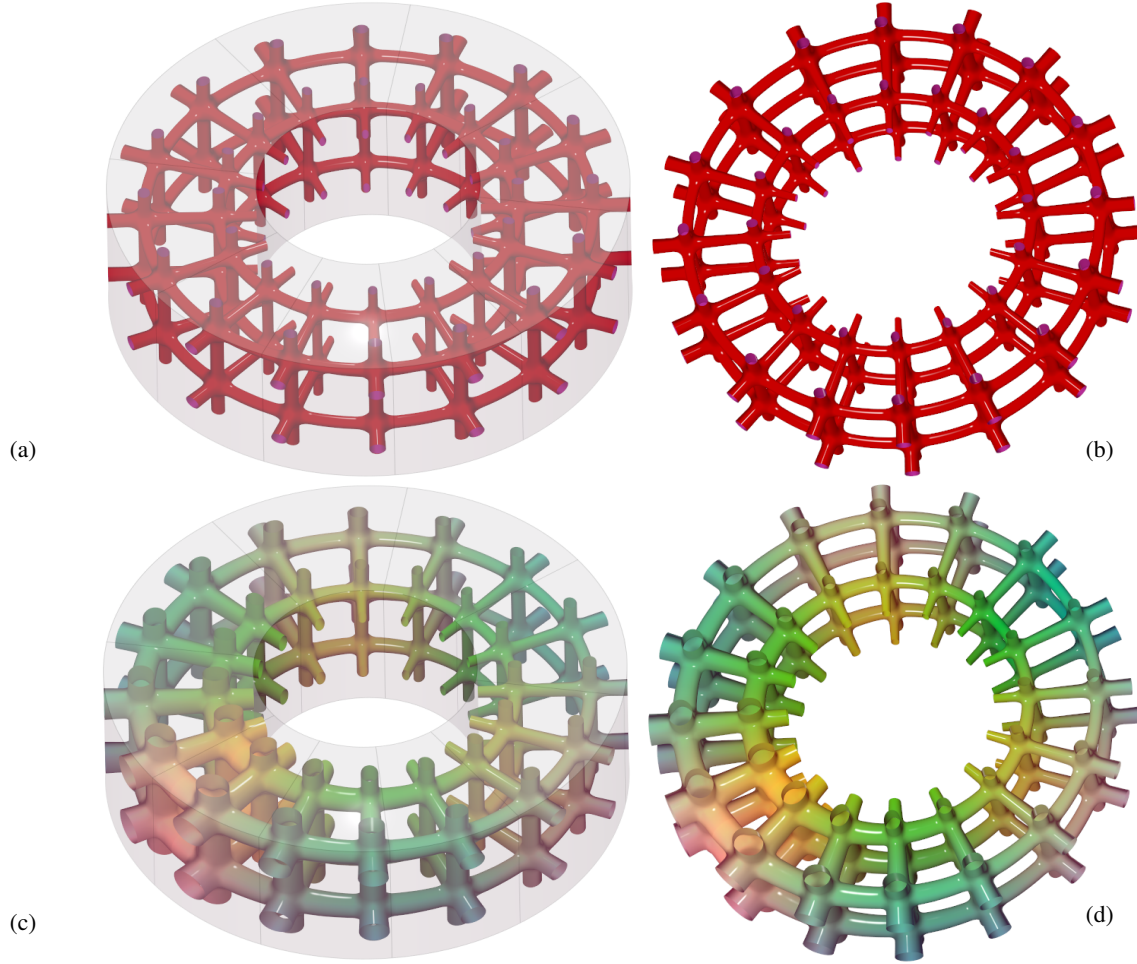


Figure 9: An embedding of an implicit B-spline 3D cross tile in a parametric B-spline torus with a square cross section, $2 \times 2 \times 16$ times (torus is shown translucent in (a) and (c)). In (a) and (b) a uniform thickness and uniform material (color) lattice is presented where as in (c) and (d), the lattice varies in both the geometry and material, independently.

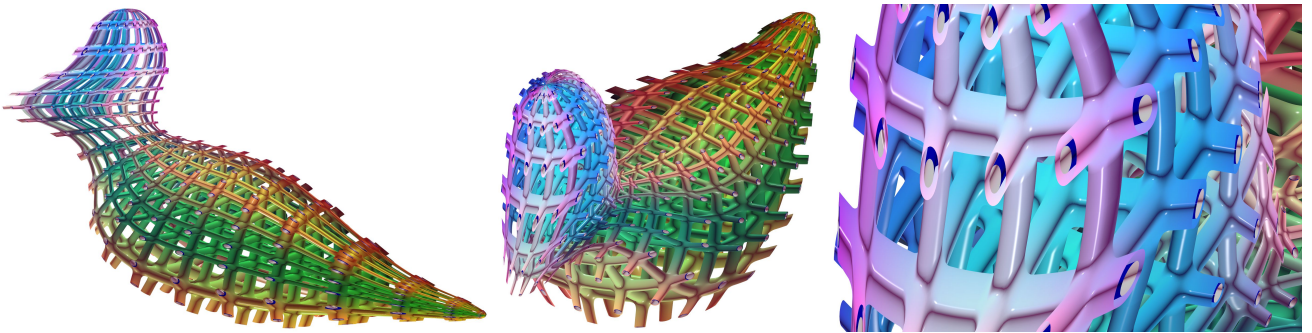


Figure 10: A heterogeneous duck macro-shape with a variable offset of an implicit cross tile.

$(10, 10, 10)$ control points in \mathbb{R}^1 , and the macro-shape is of order $(4, 2, 2)$ and has $(13, 2, 2)$ control points. For the PDE discretization we considered a background tensor-product grid with $(128, 16, 16)$ elements, coincident with the arrangement of all the implicits, and trilinear basis functions.

The displacement of the bottom surface of the tori is blocked,

while a bending distributed load $(0, 0, \alpha y)$ is applied, with $\alpha = 2 \cdot 10^{-2}$ for the case in Figure 16 (c), and $\alpha = 8.5 \cdot 10^{-2}$ for Figure 16 (d), the tori being centered at the origin and the z axis pointing upwards. While both designs present a similar amount of material (volumes are 20.82 and 21.25, respectively) and level of deformation (see the displacement magnitude fields in the corresponding figures), the geometry in Figure 16 (b) results in a much stiffer de-

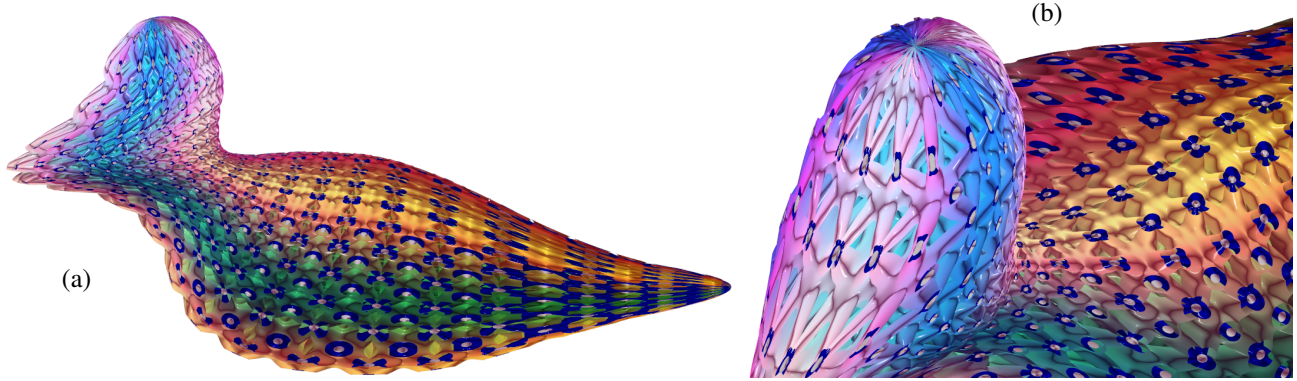


Figure 11: A heterogeneous duck macro-shape with a variable offset of an implicit tile from Figure 1.

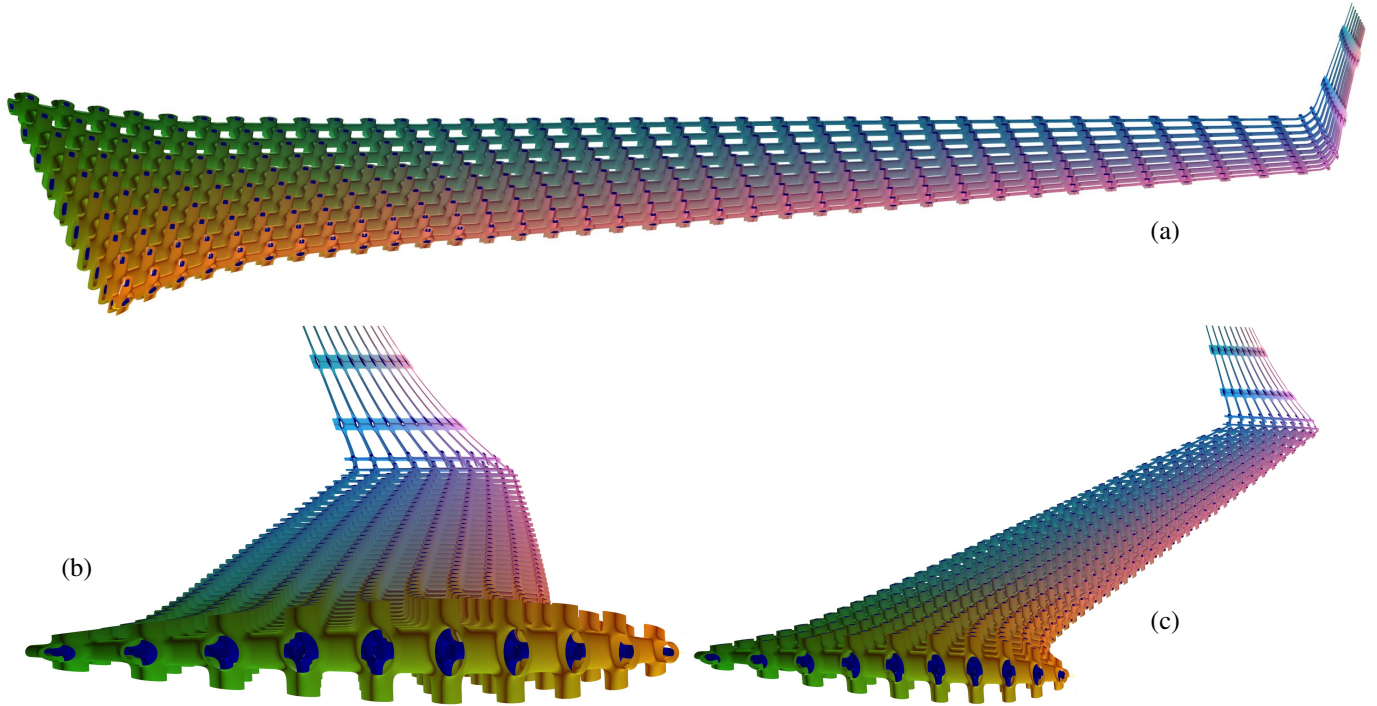


Figure 12: A heterogeneous wing macro-shape with a variable offset of an implicit cross tile.

sign, withstanding a load more than 4 times higher than the one in Figure 16 (a).

In Figure 17 another simulation with a more complex design is shown. In this case, we consider cross tile implicit trivariates mapped through a duck geometry that has orders $(3,3,3)$ and $(6,4,10)$ control points. $(18,5,4)$ tiles were placed in the parametric domain of the duck, where each cross tile trivariate has orders $(3,3,3)$ and $(10,10,10)$ control points in \mathbb{R}^1 . The tiles were created with variable distance offsets (following the algorithm in Section 3.2), and two different levels of thickness were considered (see Figures 17 (a) and 17 (b)). The elastic solution was discretized using a background tensor-product grid with $(144,40,32)$ elements, coincident with the arrangement of all the implicits, and trilinear basis functions (this grid is shown in Figure 17). In this case, the elastic displacement is blocked for the nodes of the head and tail tiles that belong to the boundary of the macro-shape, while a grav-

ity load $(0,0,-0.20)$ is applied, inducing a bending behavior in the duck as observed in Figures 17 (c) and 17 (d). As can be expected, the bulkier design (Figure 17 (d)) presents a stiffer behavior.

All simulations were run using a single processor in an Apple M2 Max chip with 64 GB of DRAM memory, using the FEniCSx open source computing platform [BDD*23, SDRW22, ALO*14], together with extra capabilities developed for dealing with unfitted discretizations that were implemented on top of the open source projects `algoim` [Say] and `customquad` [Joh]. The analysis times of these examples, without considering the time required for generating the output visualization files, were 11.4, 14.5, 89.7, and 143.8 seconds, for the cases in Figures 16 (c), 16 (d), 17 (c), and 17 (d), respectively.

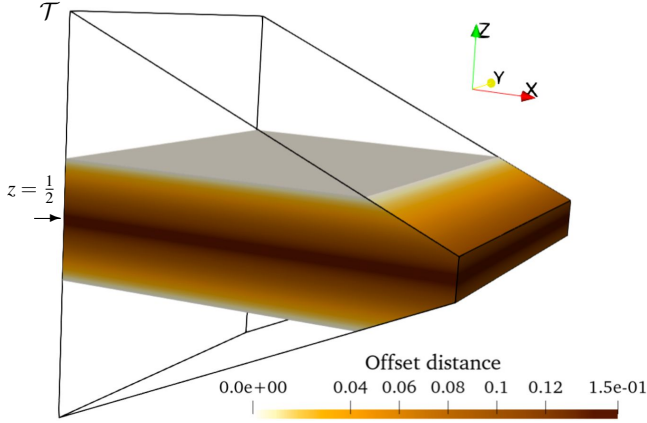


Figure 13: Linear implicit trivariate $\mathcal{I}(x, y, z) = z - 1/2$ mapped through a tapered trivariate with prescribed constant offset distance $d = 0.15$ in Euclidean lattice space on both sides of the mid-surface. Field colors represent the distance to the offset surfaces in Euclidean space.

6. Conclusions and Future Work

In this work, we have portrayed schemes to build controlled, constant and variable, offsets for implicit forms, in both the Euclidean space and even in the lattice space after the mapping through the macro-shape. Further, the use of immersive method to analyze the created 3D geometries was further presented, enabling a direct closed loop between design and analysis.

In the conventional geometric and solid modeling systems, a proper trimming of offset self-intersections has always been one of the main technical issues for a robust implementation of the underlying systems. Yet, and as demonstrated in Section 5, the use of implicit forms can alleviate this self-intersection difficulty. Though limited in resolution, the representation of distance fields in voxelized spaces has been employed as an effective solution in practice [LM14, PK08, WM13]. In this work, we have presented a B-spline-based approach that can extend the discrete representation of distance fields to a generic functional modeling of implicit fields for the synthesis and analysis of heterogeneous microstructures. The current approach introduces approximation errors in different levels and from various sources, due to the result of functional compositions over heterogeneous forms. In future work, we would like to explore the direction of systematically controlling the sampling of (procedurally defined) implicit functions and reducing the error to arbitrary precisions, suitable for specific applications under consideration.

We also plan to extend the presented simulation capabilities to the case of implicits that present heterogeneous material properties, and explore the possibility of leveraging on domain decomposition and reduced order modeling techniques to speed up the simulations for a high number of implicit tiles by exploiting the intrinsic similarities among lattices, in a similar way as in the recent work [HRAB24]. Other physics problems of interest, namely fluid dynamics, heat transfer, or waves propagation, will be also considered.

During offsets of implicits, the topology might change (as seen,

for example, in Figure 14). A possible direction to explore here is the detection and possibly the elimination of these topological changes, if so desired.

All the implicit modeling implementation parts (Section 3.1) including variable distance offsets of implicit (Section 3.2) is now part of the Irit geometric modeling kernel [Iri24] and is freely available at the source code level for non commercial use. We hope to publicly release the other portions of the implementation in the near future.

Acknowledgments

This research was supported in part by the ISRAEL SCIENCE FOUNDATION (grant No. 1817/24) and in part by the National Research Foundation of Korea (NRF) grant funded by the Korea government (MSIT) (RS-2024-00352439). Pablo Antolin acknowledges the support of the Swiss National Science Foundation through the project FLASH (No 214987). We would also like to thank anonymous reviewers for their invaluable comments.

References

- [AES*19] ABUEIDDA D. W., ELHEBEARY M., SHIANG C.-S. A., PANG S., ABU AL-RUB R. K., JASIUK I. M.: Mechanical properties of 3d printed polymeric gyroid cellular structures: Experimental and finite element study. *Materials & Design* 165 (2019), 107597. 3
- [ALO*14] ALNÆS M. S., LOGG A., ØLGAARD K. B., ROGNES M. E., WELLS G. N.: Unified form language: A domain-specific language for weak formulations of partial differential equations. *ACM Transactions on Mathematical Software* 40, 2 (2014), 1–23. 10
- [BCH*15] BURMAN E., CLAUS S., HANSBO P., LARSON M. G., MASSING A.: Cutfem: Discretizing geometry and partial differential equations. *International Journal for Numerical Methods in Engineering* 104, 7 (2015), 472–501. 6
- [BDD*23] BARATTA I., DEAN J., DOKKEN J. S., HABERA M., HALE J., RICHARDSON C., ROGNES M., SCROGGS M., SIME N., WELLS G.: Dolfinx: The next generation fenics problem solving environment. Preprint, doi.org/10.5281/zenodo.10447665, 12 2023. 10
- [BFK92] BARNHILL R. E., FROST T. M., KERSEY S. N.: *Self-Intersections and Offset Surfaces*. 1992, pp. 35–44. 2
- [BHL*16] BURMAN E., HANSBO P., LARSON M. G., MASSING A., ZAHEDI S.: Full gradient stabilized cut finite element methods for surface partial differential equations. *Computer Methods in Applied Mechanics and Engineering* 310 (2016), 278–296. 15
- [Bli82] BLINN J. F.: A generalization of algebraic surface drawing. *ACM Trans. on Graphics* 1, 3 (1982), 235–256. 2
- [Blo95] BLOOMENTHAL J.: *Introduction to Implicit Surfaces*. Morgan Kaufmann, 1995. 2
- [BPV20] BUFFA A., PUPPI R., VÁZQUEZ R.: A minimal stabilization procedure for isogeometric methods on trimmed geometries. *SIAM Journal on Numerical Analysis* 58, 5 (2020), 2711–2735. 15
- [BVM18] BADIA S., VERDUGO F., MARTÍN A. F.: The aggregated unfitted finite element method for elliptic problems. *Computer Methods in Applied Mechanics and Engineering* 336 (2018), 533–553. 6
- [CRE01] COHEN E., RIESENFELD R., ELBER G.: *Geometric Modeling with Splines: An Introduction*. AK Peters, Wellesley, MA, 2001. 2
- [dPVvB*23] DE PRENTER F., VERHOOSSEL C., VAN BRUMMELEN E., LARSON M., S. B.: Stability and conditioning of immersed finite element methods: analysis and remedies. *Archives of Computational Methods in Engineering* 30 (2023), 3617–3656. 15

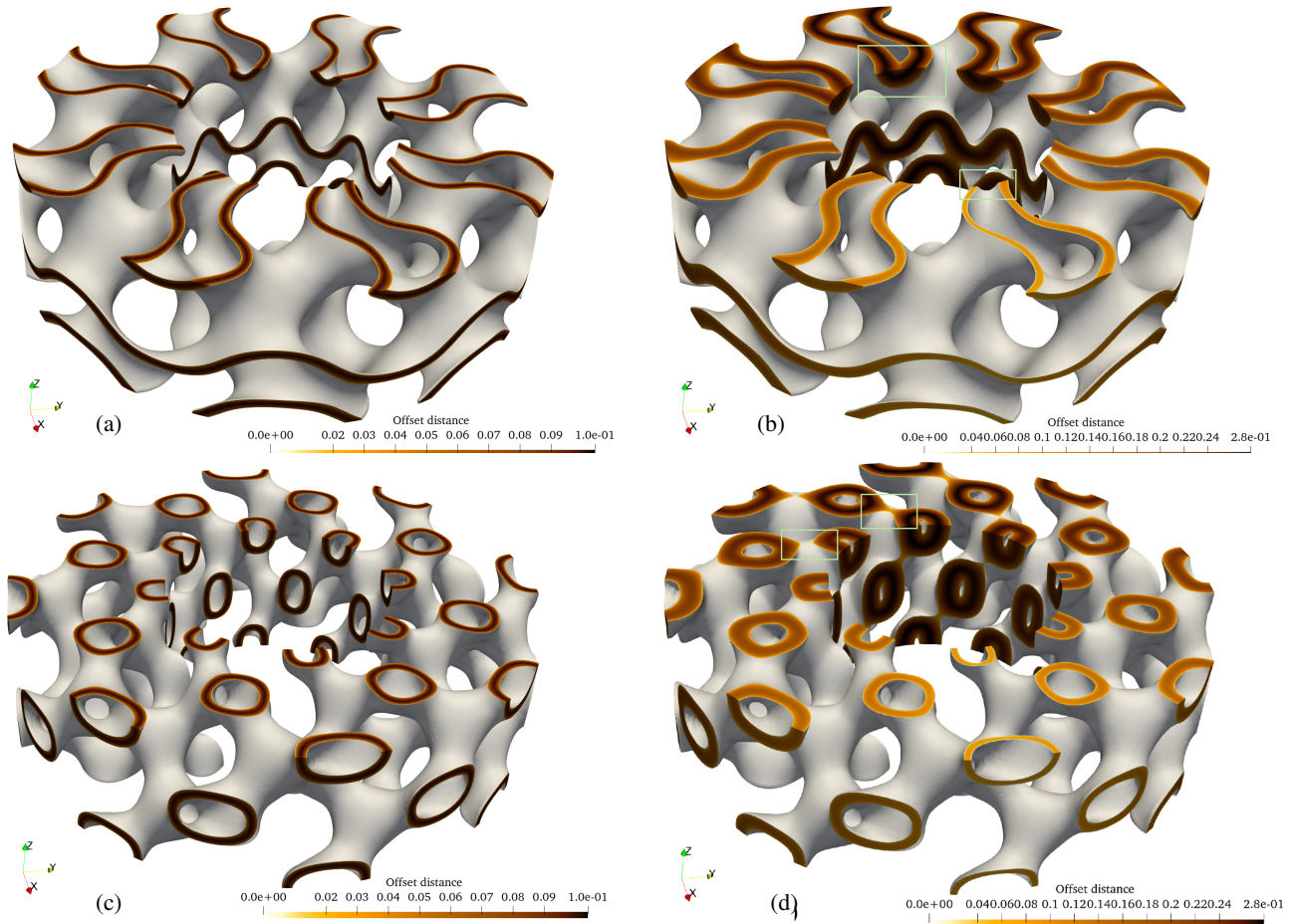


Figure 14: Schoen's gyroid (a)-(b) and Scharwz's diamond (c)-(d) implicit trivariates in a torus macro-shape with square cross section and prescribed offset distances in Euclidean space: (a)-(c) constant distance and (b)-(d) variable distance. Note in (b) and (d), the smooth topological changes in the offsets, where no self-intersection processing is required - compare each two marked rectangles for the proper topological change in both small and large offset amounts, in these variable offset examples. The brown field colors represent the distance to the offset surfaces in Euclidean space.

- [DPYR08] DÜSTER A., PARVIZIAN J., YANG Z., RANK E.: The finite cell method for three-dimensional problems of solid mechanics. *Computer Methods in Applied Mechanics and Engineering* 197, 45 (2008), 3768–3782. [6](#), [15](#)
- [Elb23] ELBER G.: A review of a b-spline based volumetric representation: Design, analysis and fabrication of porous and/or heterogeneous geometries. *Computer-Aided Design* 163 (2023), 103587. [1](#)
- [ELK97] ELBER G., LEE I.-K., KIM M.-S.: Comparing offset curve approximation methods. *IEEE Computer Graphics and Applications* 17, 3 (1997), 62–71. [3](#)
- [Far08] FAROUKI R.: *Pythagorean-Hodograph Curves*. Springer, Berlin, 2008. [2](#)
- [FLLF21] FENG J., LIU B., LIN Z., FU J.: Isotropic porous structure design methods based on triply periodic minimal surfaces. *Materials & Design* 210 (2021), 110050. [2](#)
- [GCDL22] GAO D., CHEN J., DONG Z., LIN H.: Connectivity-guaranteed porous synthesis in free form model by persistent homology. *Computers & Graphics* 106 (2022), 33–44. [2](#)
- [GGL24] GAO D., GAO Y., LIN H.: Periodic implicit representation, design and optimization of porous structures using periodic b-splines. *arXiv preprint arXiv:2402.12076* 171 (2024), 103703. [2](#)
- [HE21] HONG Q. Y., ELBER G.: Conformal microstructure synthesis in trimmed trivariate based v-reps. *Computer-Aided Design* 140 (2021), 103085. [2](#)
- [HEK23] HONG Q. Y., ELBER G., KIM M.-S.: Implicit functionally graded conforming microstructures. *Computer-Aided Design* 162 (2023), 103548. [2](#), [3](#), [4](#)
- [HL93] HOSCHKE J., LASSER D.: *Fundamentals of Computer Aided Geometric Design*. AK Peters, Wellesley, MA, 1993. [2](#)
- [HL21] HU C., LIN H.: Heterogeneous porous scaffold generation using trivariate b-spline solids and triply periodic minimal surfaces. *Graphical Models* 115 (2021), 101105. [2](#), [5](#)
- [Hof89] HOFFMANN C.: *Geometric & Solid Modeling: An Introduction*. Morgan Kaufmann, 1989. [2](#)
- [HPKE19] HONG Q. Y., PARK Y., KIM M.-S., ELBER G.: Trimming offset surface self-intersections around near-singular regions. *Computers & Graphics* 82 (2019), 84–94. [3](#)
- [HRAB24] HIRSCHLER T., R. BOUCLIER, ANTOLIN P., BUFFA A.: Reduced order modeling based inexact feti-dp solver for lattice structures. *International Journal for Numerical Methods in Engineering* e7419 (2024). [11](#)
- [Hug00] HUGHES T.: *The finite element method: linear static and dy-*

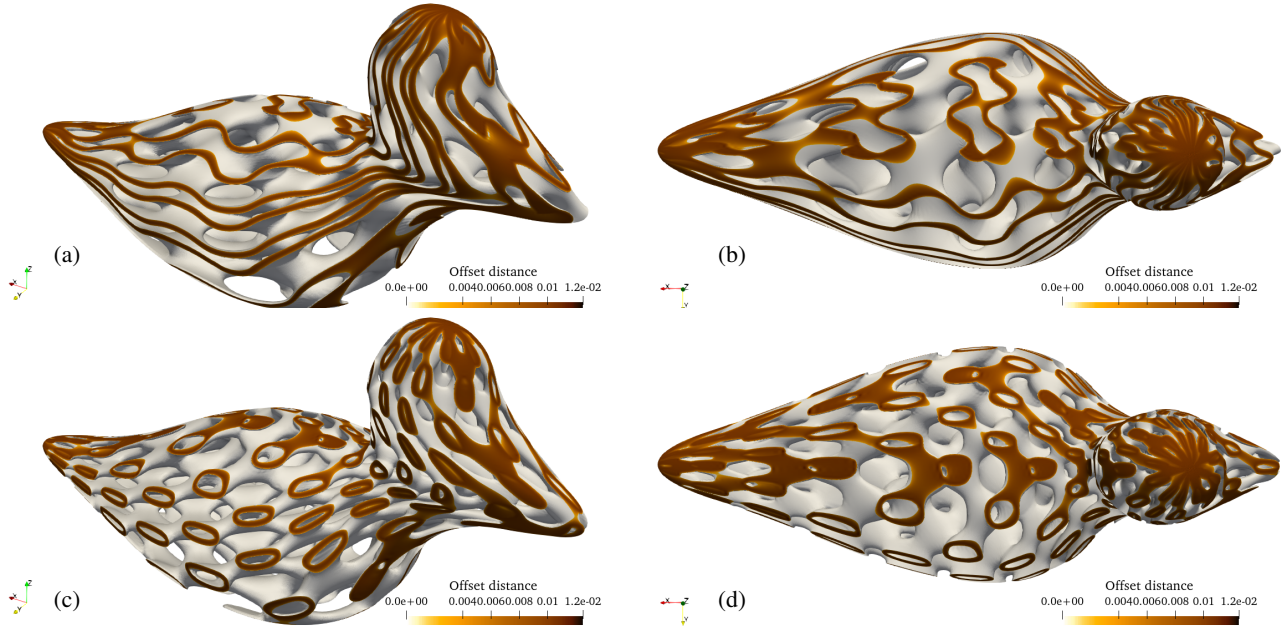


Figure 15: Schoen's gyroid (a)-(b) and Scharwz's diamond (c)-(d) implicit trivariates in a duck macro-shape with constant offset distances in Euclidean space: (a)-(c) perspective and (b)-(d) top view. The brown Field colors represent the distance to the offset surfaces in Euclidean space.

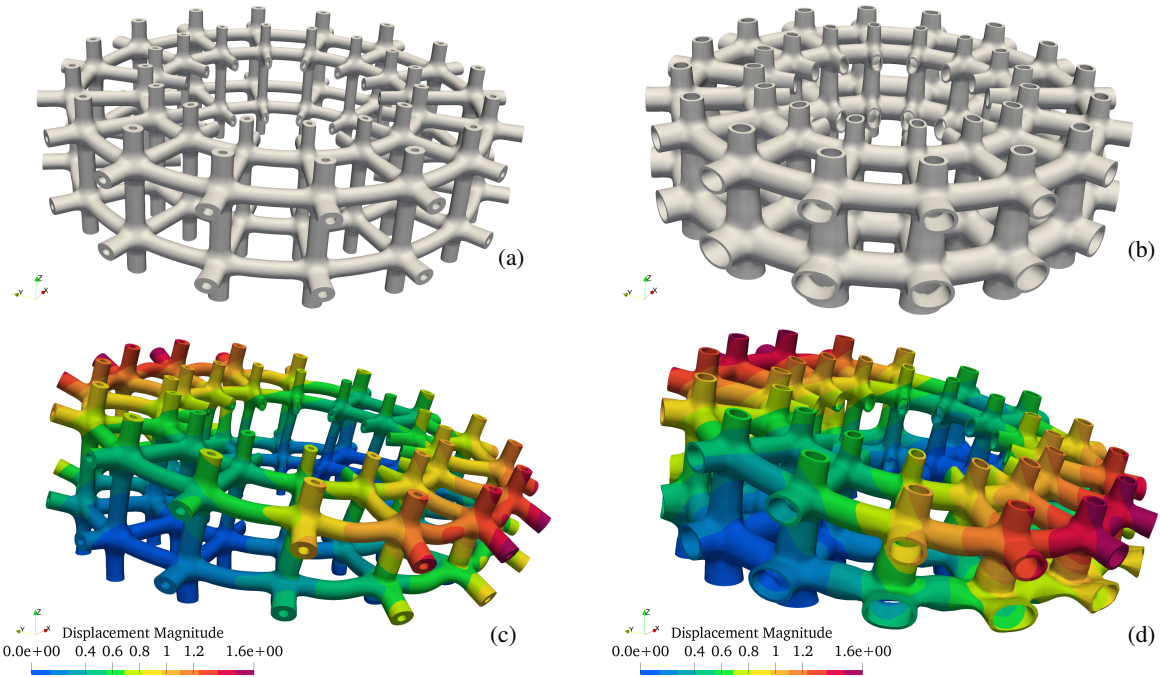


Figure 16: Simulation of TPMS implicit trivariates, in a torus with square cross section: In (a)-(b) two different sets of tiles are considered. Their bottom faces are fixed and bending distributed loads are applied. Their deformed configurations with elastic deformation fields are depicted in (c)-(d), respectively.

namic finite element analysis. Dover Publications, Mineola, NY, 2000. 6

[Iri24] IRIT: The irit geometric modeling environment., 2024. <http://www.cs.technion.ac.il/~gershon/irit>. 11

[Joh] JOHANSSON A.: Customquad. <https://github.com/augustjohansson/ustomquad>. 10

[KAH*21a] KORSHUNOVA N., ALAIMO G., HOSSEINI S., CAR-RATURO M., REALI A., NIIRANEN J., AURICCHIO F., RANK E., KOLLMANNSSBERGER S.: Bending behavior of octet-truss lattice structures: Modelling options, numerical characterization and experimental validation. *Materials & Design* 205 (2021), 109693. 3

[KAH*21b] KORSHUNOVA N., ALAIMO G., HOSSEINI S., CAR-RATURO M., REALI A., NIIRANEN J., AURICCHIO F., RANK E.,

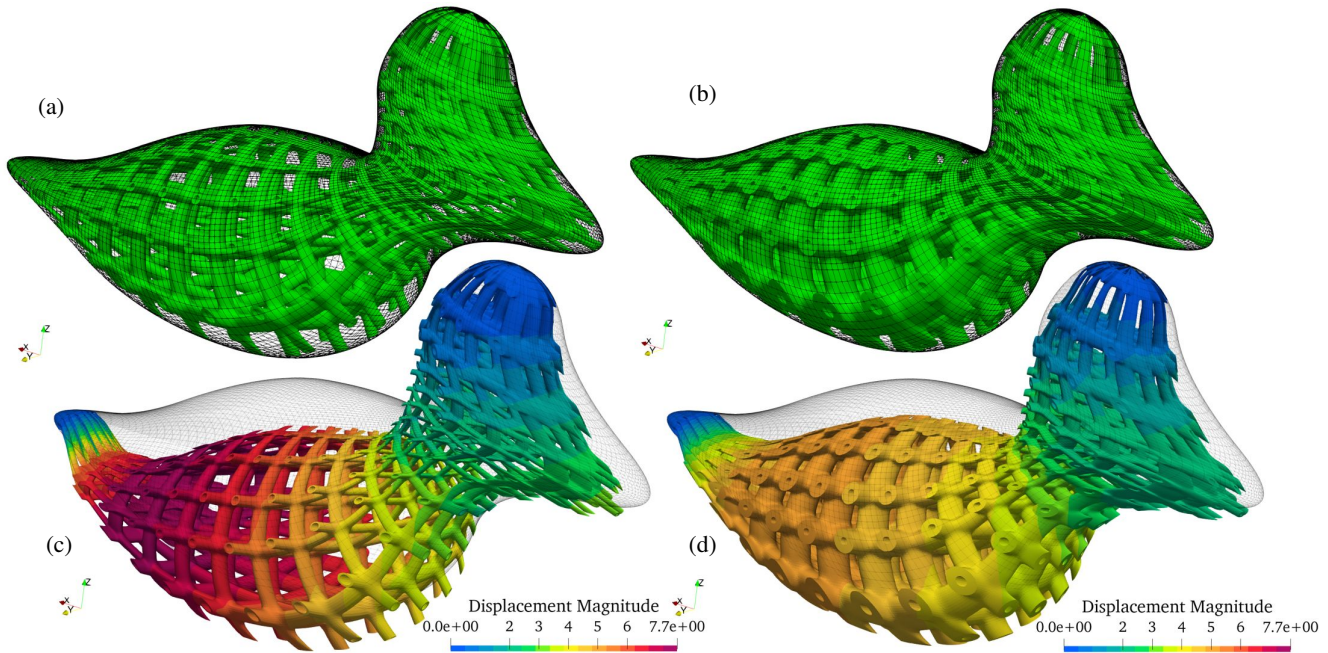


Figure 17: Simulation of TPMS implicit trivariates in a duck macro-shape: (a) and (b) show the implicit geometries immersed in the solution background mesh and (c) and (d) presents the deformed geometries with elastic deformation field. Two different cross tiles were considered: thinner in (a) and (c), and thicker in (b) and (d). For the simulations in (c) and (d), the external faces of the duck's tale and the top part of the head are fixed, and the same vertical gravity load is applied in the whole body.

- KOLLMANNBERGER S.: Image-based numerical characterization and experimental validation of tensile behavior of octet-truss lattice structures. *Additive Manufacturing* 41 (2021), 101949. [3](#)
- [KHL19] KOCHMANN D., HOPKINS J., L. VALDEVIT: Multiscale modeling and optimization of the mechanics of hierarchical metamaterials. *MRS Bulletin* 44, 10 (2019), 773–781. [3](#)
- [LAR*21] LEHDER E., ASHCROFT A., R. WILDMAN, L. RUIZ-CANTU, I. MASKERY: A multiscale optimisation method for bone growth scaffolds based on triply periodic minimal surfaces. *Biomechanics and Modeling in Mechanobiology* 20 (2021), 2085–2096. [2](#)
- [LC87] LORENSEN W. E., CLINE H. E.: Marching cubes: A high resolution 3d surface construction algorithm. *Computer Graphics (SIGGRAPH'87 Proc.)* 21, 4 (1987), 163–169. [1](#)
- [LM14] LI W., MCMAINS S.: A sweep and translate algorithm for computing voxelized 3d minkowski sums on the gpu. *Computer-Aided Design* 46 (2014), 90–100. [3](#), [11](#)
- [Mae99] MAEKAWA T.: An overview of offset curves and surfaces. *Computer-Aided Design* 31, 3 (1999), 165–173. [3](#)
- [MAE19] MASSARWI F., ANTOLIN P., ELBER G.: Volumetric untrimming: Precise decomposition of trimmed trivariates into tensor products. *Computer Aided Geometric Design* 71 (2019), 1–15. [2](#)
- [ME16] MASSARWI F., ELBER G.: A b-spline based framework for volumetric object modeling. *Computer-Aided Design* 78 (2016), 36–47. [2](#)
- [MMAE18] MASSARWI F., MACHCHHAR J., ANTOLIN P., ELBER G.: Hierarchical, random and bifurcation tiling with heterogeneity in microstructures construction via functional composition. *Computer-Aided Design* 102 (2018), 148–159. [2](#)
- [MS18] MAIN A., SCOVAZZI G.: The shifted boundary method for embedded domain computations. part i: Poisson and stokes problems. *Journal of Computational Physics* 372 (2018), 972–995. [6](#)
- [MSA*18] MASKERY I., STURM L., AREMU A., PANESAR A., WILLIAMS C., TUCK C., WILDMAN R., ASHCROFT I., HAGUE R.: Insights into the mechanical properties of several triply periodic minimal surface lattice structures made by polymer additive manufacturing. *Polymer* 152 (2018), 62–71. [2](#)
- [nTo] NTOPOLOGY:.. <https://www.ntop.com>. [2](#)
- [PFV*11] PASKO A., FRYAZINOV O., VILBRANDT T., FAYOLLE P.-A., ADZHIEV V.: Procedural function-based modelling of volumetric microstructures. *Graphical Models* 73, 5 (2011), 165–181. [2](#)
- [PK08] PAVIC D., KOBELT L.: High-resolution volumetric computation of offset surfaces with feature preservation. *Computer Graphics Forum* 27, 2 (2008), 165–174. [3](#), [11](#)
- [RR86] ROSSIGNAC J. R., REQUICHA A. A.: Offsetting operations in solid modelling. *Computer Aided Geometric Design* 3, 2 (1986), 129–148. [2](#)
- [Say] SAYE R. I.: Algoim, algorithms for implicitly defined geometry, level set methods, and voronoi implicit interface methods. <https://algoim.github.io>. [6](#), [10](#), [15](#)
- [Say14] SAYE R. I.: High-order methods for computing distances to implicitly defined surfaces. *Communications in Applied Mathematics and Computational Science* 9, 1 (2014), 107–141. [6](#)
- [Say15] SAYE R. I.: High-order quadrature methods for implicitly defined surfaces and volumes in hyperrectangles. *SIAM Journal on Scientific Computing* 37, 2 (2015), A993–A1019. [6](#), [15](#)
- [Say22] SAYE R. I.: High-order quadrature on multi-component domains implicitly defined by multivariate polynomials. *Journal of Computational Physics* 448 (2022), 110720. [6](#), [15](#)
- [SDRW22] SCROGGS M. W., DOKKEN J. S., RICHARDSON C. N., WELLS G. N.: Construction of arbitrary order finite element degree-of-freedom maps on polygonal and polyhedral cell meshes. *ACM Transactions on Mathematical Software* 48, 2 (2022), 18:1–18:23. [10](#)
- [Sol] SOLUTIONS I.: Immersed method of moments™ (imm). <https://intact-solutions.com/rev/2023/06/immersed-method-of-moments-imm>. [3](#)

- [WGG99] WYVILL B., GUY A., GALIN E.: Extending the csg tree. warping, blending and boolean operations in an implicit surface modeling system. *Computer Graphics Forum* 18, 2 (1999), 149–158. 2
- [WJH*22] WANG S., JIANG Y., HU J., FAN X., LUO Z., LIU Y., LIU L.: Efficient representation and optimization of tpms-based porous structures for 3d heat dissipation. *Computer-Aided Design* 142 (2022), 103123. 1
- [WM13] WANG C. C., MANOCHA D.: Gpu-based offset surface computation using point samples. *Computer-Aided Design* 45, 2 (2013), 321–330. 3, 11
- [WRC*20] WANG Y., REN X., CHEN Z., JIANG Y., CAO X., FANG S., ZHAO T., LI Y., FANG D.: Numerical and experimental studies on compressive behavior of gyroid lattice cylindrical shells. *Materials & Design* 186 (2020), 108340. 3
- [YL23] YAN J., LIN H.: Reasonable thickness determination for implicit porous sheet structure using persistent homology. *Computers & Graphics* 115 (2023), 236–245. 2
- [YRL*19] YAN X., RAO C., LU L., SHARF A., ZHAO H., CHEN B.: Strong 3d printing by tpms injection. *IEEE Transactions on Visualization and Computer Graphics* 26, 10 (2019), 3037–3050. 2
- [ZBQC13] ZANNI C., BERNHARDT A., QUIBLIER M., CANI M.-P.: Scale-invariant integral surfaces. *Computer Graphics Forum* 32, 8 (2013), 219–232. 2
- [ZEE23] ZWAR J., ELBER G., ELGETI S.: Shape optimization for temperature regulation in extrusion dies using microstructures. *The Journal of Mechanical Design* 145, 1 (2023), 012004. 1
- [Zha05] ZHAO H.: A fast sweeping method for eikonal equations. *Mathematics of Computation* 74, 250 (2005), 603–627. 2

Appendix A: Simulation

The finite element unfitted discretization paradigm briefly introduced in Section 4 allows to decouple the domain definition from the solution discretization, that is based on a background grid independent from the geometry, what offers great flexibility. Nevertheless, this flexibility does not come for free. Unfitted methods present a series of challenges as, for instance: the need of imposing essential (Dirichlet) boundary conditions in a weak sense through Nitsche-like methods, and the possible stability problems associated with their imposition (see, e.g., [BPV20]); the possible ill-conditioning of the resulting linear system associated with the potentially arbitrary small contribution of some cut basis functions [dPVvB*23]; or the computation of integrals over cut elements in \mathcal{G}_{cut} , that will be addressed below.

In order to better illustrate the method, we focus on a linear elasticity problem, that is governed by a variational problem of the form:

$$\int_{\Omega} \sigma(u) : \varepsilon(v) dx = \int_{\Omega} f \cdot v dx + \int_{\Gamma_N} t \cdot v dx, \quad (14)$$

where $u : \Omega \rightarrow \mathbb{R}^3$ is the elastic deformation field, and $v : \Omega \rightarrow \mathbb{R}^3$ the associated test or virtual deformation; $\varepsilon(v) = \nabla^s v$ is the infinitesimal strain tensor and $\sigma(u) = 2\mu \varepsilon(u) + \lambda \text{tr}(\varepsilon(u))I$ the Cauchy stress tensor, being λ and μ the Lamé material parameters; finally, $f : \Omega \rightarrow \mathbb{R}^3$ is the distributed body load and $t : \Gamma_N \rightarrow \mathbb{R}^3$ the applied traction (Neumann) boundary condition on a boundary subset $\Gamma_N \subset \partial\Omega$. In this setting, and for the sake simplicity, we assumed that prescribed displacements (Dirichlet) boundary conditions are only applied on $\Gamma_D \subset \partial\Omega \cap \partial\mathcal{G}$, such that $\Gamma_D = \partial\Omega \setminus \Gamma_N$, and therefore can be enforced strongly.

Remark A.1 In the numerical examples presented in Section 5, the domain Ω was defined through implicit in the parametric space D of a macro-shape \mathcal{T} that maps them into the Euclidean space. In such a case, the PDE at hand is discretized by means of a Cartesian grid \mathcal{G} covering D , and, consequently, the integrals in (14) must be pulled-back from the Euclidean to the parametric space through \mathcal{T}^{-1} .

After discretizing u and v in the active part of the background grid, i.e., in $\mathcal{G}_{\text{in}} \cup \mathcal{G}_{\text{cut}}$,[¶] Equation (14) yields a linear system of equations whose resolution gives the coefficients of the approximated PDE solution. Nonetheless, in order to assemble the system, the integrals involved must be precisely evaluated inside Ω . Thus, these integrals can be computed element-wise for a generic quantity $\alpha : \Omega \rightarrow \mathbb{R}$ as:

$$\int_{\Omega} \alpha(x) dx = \sum_{Q \in \mathcal{G}_{\text{in}}} \int_Q \alpha(x) dx + \sum_{Q \in \mathcal{G}_{\text{cut}}} \int_{Q \cap \Omega} \alpha(x) dx. \quad (15)$$

For the first term, the integrals over \mathcal{G}_{in} are evaluated in a standard way by means of Gauss-Legendre quadrature rules. On the other hand, the integrals over the active part of the cut elements, i.e., $\mathcal{G}_{\text{cut}} \cap \Omega$, require special treatment. By leveraging on the implicit definition of the domain Ω described in previous sections, we create custom quadrature rules for every single element in \mathcal{G}_{cut} by using the methods proposed in [Say15, Say22] (through their implementation in [Say]). These methods provide highly accurate and efficient quadrature rules when compared with classical alternatives as, for instance, octree based approaches [DPYR08]. The same algorithms are applied for boundary integrals.

Remark A.2 In order to mitigate the possible ill-conditioning of the linear system of equations caused by arbitrary small cut elements, as proposed in [BHL*16], we add an additional stabilization term to Equation (14), namely, $\int_{\mathcal{G}_{\text{cut}} \setminus \Omega} \sigma(u) : \varepsilon(v) dx$. As detailed in that work, this stabilization results in a uniform bound on the linear system's condition number for any discretization degree $p \geq 1$, while preserves full order of convergence of the numerical scheme only for $p = 1$.

[¶] The degrees-of-freedom associated with basis functions whose support only intersect \mathcal{G}_{out} are not considered in the problem.